RC2:

This manuscript presents a one-year observational study of new particle formation (NPF) events and their impact on cloud condensation nuclei (CCN) in a Chinese coastal city. A total of 46 NPF events were identified, representing an overall frequency of 12.7%. The study provides a detailed seasonal analysis of NPF characteristics, including particle formation rates (FR), growth rates (GR), and their interactions with atmospheric chemistry and aerosol composition. The results reveal pronounced seasonal contrasts. For example, spring shows the highest FR and NPF frequency but exhibits suppressed particle growth and negligible CCN enhancement; in contrast, summer demonstrates the highest GR and the most significant CCN enhancement effect. While the findings are interesting, the manuscript consists largely of measurement results, which may be more suitable for publication as a measurement report unless the authors can substantially expand on the novelty of the study beyond data reporting. Specific comments are provided below:

Response: We appreciate the time and effort that the editor and the reviewers dedicated to providing feedback on our manuscript. We are grateful for the insightful comments and valuable improvements to our paper. We have incorporated most of the suggestions made by the reviewers. According to your suggestion, we modified the manuscript in detail and marked the revised contents with red font.

1. Observation sites: The methods describe measurements from two distinct sites: the Fujian Provincial Environmental Monitoring Center Station (central urban) and the Fuzhou Meteorological Bureau Station (near the river, southern urban). However, the results and discussion present integrated or representative data without clarifying how data from these two locations were merged, compared, or selected for the analyses in Figures 3–7. These locations are potentially subject to different local influences (e.g., intense human activity vs. marine/river impacts). The authors have missed an opportunity to use the dual-site setup to examine local influences. Were any differences observed? Please clarify.

Response: We thank the reviewer for this constructive comment.

1) The two original observation sites are only about 8 km apart (urban: 26.11°N, 119.30°E; riverside: 26.05°N, 119.26°E), so their local environments are not expected to be drastically different. Because the two sites measured completely different variables (aerosol chemistry at the urban station vs. CCN and meteorology at the riverside station), no overlapping measurements exist for direct comparison. Therefore, we selected the national monitoring station near the meteorological bureau (1282A, representing the riverside area) and compared it with the station at the Environmental Monitoring Center (1283A, representing the urban area). Using data from 46 NPF event days (as identified at the urban station), we compared six pollutants ($PM_{2.5}$, NO_2, O_3, PM_{10}, SO_2, and CO). The results are presented in Table S2. The two sites show generally comparable pollutant levels, reflecting a well-mixed regional background. Nevertheless, the urban site exhibits slightly higher NO_2 (+4.7%) and CO (+4%), indicating a modest anthropogenic influence, while the riverside site has marginally higher $PM_{2.5}$ and PM_{10}, possibly due to local sources or humidity effects. These small differences confirm that the two sites are subject to distinct local influences (urban vs. riverside), as noted by the reviewer. We have added this discussion in Section 2.1 (Lines 156–160).

   Line 156-160: Given the short distance (about 8 km) and the regional background homogeneity, the local environments of the two sites are not expected to be drastically different, although each is influenced by its specific surroundings (urban vs. riverside). A comparison of air pollutant concentrations between the two sites using nearby national monitoring stations (Supplement Table S2).

Table S2. Comparison of air pollutant concentrations at the two sites during NPF event days (mean ± standard deviation, n = 46 days).

Factors	Riverside site (1282A)	Urban site (1283A)	Difference (%)
$PM_{2.5}$ (μg/m³)	19.6±9.7	17.6±8.7	–10.2
NO_2 (μg/m³)	19.3±6.8	20.2±8.5	+4.7

O_3 (μg/m³)	61.4±19.5	61.8±18.3	+0.7
PM_{10} (μg/m³)	38.3±14.0	37.6±13.8	–1.8
SO_2 (μg/m³)	3.9±1.2	3.9±1.0	0
CO (mg/m³)	0.50±0.10	0.52±0.15	+4

2) All raw measurements (aerosol size distribution, chemical composition, BC, etc.) were obtained from the instruments listed in Table S1, with their respective observation sites indicated in the table. The derived parameters (FR, GR, CS, κ_inorg, etc.) were then calculated from these raw data following the methods in Section 2.3. Specifically, all data used in Figures 3–7 (WPS-1000, MARGA, OC/EC, AE-33) come from the Urban Environmental Monitoring Center. The CCN data from the meteorological bureau station (riverside site) are used only in later sections (Figures 8–9), and meteorological data are used only for contextual interpretation. The two stations measure different variables. The comparison results in Table S2 confirm that the regional background is well mixed, supporting the representativeness of the urban-site data used in Figures 3–7.

Table S1. Summary of measurement instruments, parameters, time resolution, averaging time used for analysis, and measurement uncertainties.

Station	Instrument	Parameter(s)	Time resolution	Uncertainty
The Fujian Provincial Environmental Monitoring Center Station	WPS-1000	Aerosol size distribution (10–350 nm)	6 min	±10%
	AE-33	BC	1 h	±10% (Drinovec et al., 2015)
	OC/EC Analyzer	OC, EC	1 h	OC: ±3.6%; EC: ±6.8% (Zhang et al., 2021)
	MARGA (ADI 2080)	SO_4^{2-}, NO_3^-, NH_4^+, Na^+, K^+, Ca^{2+}, Cl^-; NH_3, HNO_2, HNO_3, HCl, SO_2	1h	±5–20% (Battelle, 2009)
The Fuzhou Meteorological Bureau Station	Meteorological station	T, RH, WS, WD, precipitation	1 h	T: ±0.2°C; RH: ±4–8%; WS: ±(0.5+0.03v) m/s; WD: ±5°; precip.: ±0.4 mm/±4%
	CCNC-100	CCN number concentration and spectrum distribution	10 min per SS	±10%

Reference:

Battelle: Environmental Technology Verification Report: Applikon MARGA Semi-Continuous Ambient Air Monitoring System, U.S. Environmental Protection Agency, available at: https://nepis.epa.gov/Exe/ZyPURL.cgi?Dockey=P100FZOD.pdf (last access: 24 April 2026), 2009.

Drinovec, L., Močnik, G., Zotter, P., Prévôt, A. S. H., Ruckstuhl, C., Coz, E., Rupakheti, M., Sciare, J., Müller, T., Wiedensohler, A., and Hansen, A. D. A.: The "dual-spot" aethalometer: an improved measurement of aerosol black carbon with real-time loading compensation, Atmos. Meas. Tech., 8, 1965–1979, https://doi.org/10.5194/amt-8-1965-2015, 2015.

Zhang, X., Trzepla, K., White, W., Raffuse, S., and Hyslop, N. P.: Intercomparison of thermal–optical carbon measurements by Sunset and Desert Research Institute (DRI) analyzers using the IMPROVE_A protocol, Atmos. Meas. Tech., 14, 3217–3231, https://doi.org/10.5194/amt-14-3217-2021, 2021.

2. Line 151: The constant A is given as 1.37×10^{-7} $h\cdot cm^{-3}\cdot nm^{-1}$. Please provide a reference for this value.

Response: We thank the reviewer for pointing out this missing reference. The constant $A=1.37\times10^{-7} h\cdot cm^{-3}\cdot nm^{-1}$ is taken from (Maso et al., 2005). In that paper, the authors derived this constant based on the molecular properties of sulfuric acid (vapor molecular weight, diffusion coefficient, and density) under the assumption that particle growth is driven solely by condensation of a low-volatility vapor. Specifically, the constant A is obtained by integrating the mass flux equation and relates the observed growth rate GR to the vapor concentration C via $C=A\times GR$. The same value has been widely used in subsequent NPF studies (Kulmala et al., 2012; Nieminen et al., 2010). We have now added the citation to Dal Maso et al. (2005) in the revised manuscript. The sentence now reads:

Line 205-206: where Dp is the particle diameter, and A is a constant, which has the value 1.37×10^{-7} $h\cdot cm^{-3}\cdot nm^{-1}$ for a vapor with molecular properties of sulfuric acid (Dal

Maso et al., 2005).

Reference:

Kulmala, M., Petäjä, T., Nieminen, T., Sipilä, M., Manninen, H. E., Lehtipalo, K., Dal Maso, M., Aalto, P. P., Junninen, H., Paasonen, P., Riipinen, I., Lehtinen, K. E. J., Laaksonen, A., and Kerminen, V.-M.: Measurement of the nucleation of atmospheric aerosol particles, Nat. Protoc., 7, 1651–1667, https://doi.org/10.1038/nprot.2012.091, 2012.

Maso, M. D., Kulmala, M., Riipinen, I., Wagner, R., Hussein, T., Aalto, P., and Lehtinen, K.: Formation and growth of fresh atmospheric aerosols: eight years of aerosol size distribution data from SMEAR II, hyytiälä, finland, Boreal Environ. Res., 2005.

Nieminen, T., Lehtinen, K. E. J., and Kulmala, M.: Sub-10 nm particle growth by vapor condensation – effects of vapor molecule size and particle thermal speed, Atmos. Chem. Phys., 10, 9773–9779, https://doi.org/10.5194/acp-10-9773-2010, 2010.

3. Lines 152–159: The calculation of the hygroscopicity parameter κ (Equation 6) assumes an internal mixture of organics, $(NH_4)_2SO_4$, and NH_4NO_3. Although this is a common simplification, the authors should briefly acknowledge this assumption and its limitations. Specifically, neglecting other inorganic ions (e.g., Cl^-, sea-salt components, which may be relevant in a coastal city) and assuming immediate mixing could affect the accuracy of the derived κ values, especially in discussions of seasonal hygroscopicity contrasts.

Additionally, while the method section provides κ values for pure $(NH_4)_2SO_4$ (0.61) and NH_4NO_3 (0.67), it does not specify the κ value assigned to the organic component. This is a required input for the calculation. Please clarify.

Response: We sincerely thank the reviewer for this insightful comment. In our original analysis, we followed a common approach that was originally developed for inland sites where chloride concentrations are typically low, and therefore, we did not include Cl^- in the hygroscopicity calculation. However, as the reviewer rightly pointed out, Fuzhou

is a coastal city where Cl^- may contribute non-negligibly to aerosol composition. We acknowledge that our previous treatment was an oversimplification for this specific environment.

Following the reviewer's suggestion, we have now fully revised the calculation of the hygroscopicity parameter. Specifically, we have incorporated Cl^- into the ion-pairing scheme following Gysel et al. (2007) and Kuang et al. (2020). The measured concentrations of SO_4^{2-}, NO_3^-, NH_3^+, and Cl^- are now used to form NH_4Cl, $(NH_4)_2SO_4$, NH_4HSO_4, and NH_4NO_3 sequentially. This allows us to derive a revised inorganic hygroscopicity parameter (κ_{inorg}) that better reflects the aerosol properties in the coastal atmosphere of Fuzhou.

At the same time, we have clarified in the revised manuscript that our calculation only represents the inorganic fraction. Because we lack volume fraction data for organic species, we do not assign a κ value to organics, and we therefore explicitly state that κ_{inorg} should be considered as an upper-limit estimate of total aerosol hygroscopicity. We have also corrected the misleading wording that previously suggested an internal mixture including organics, and we now clearly discuss the limitations of the internal mixing assumption.

Line 216-228:

Hygroscopicity parameter (κ_{inorg}) for inorganic species. Due to the lack of organic composition measurements, we estimated the hygroscopicity of the inorganic fraction only. The measured water-soluble ions (SO_4^{2-}, NO_3^-, NH_4^+, Cl^-) were converted to mass concentrations of inorganic salts using the ion-pairing scheme described in Gysel et al. (2007) and Kuang et al. (2020). The following salts and their κ values (Kuang et al., 2020) were considered: $(NH_4)_2SO_4$ ($\kappa = 0.48$), NH_4NO_3 ($\kappa = 0.58$), NH_4HSO_4 ($\kappa = 0.56$), and NH_4Cl ($\kappa = 0.93$). The volume fraction of each salt was calculated using its density (also from Kuang et al., 2020). The overall inorganic hygroscopicity parameter κ_{inorg} was then obtained by volume-weighted mixing (Petters and Kreidenweis, 2007):

$$\kappa_{inorg} = \sum_i \varepsilon_i \kappa_i \quad (7)$$

where κ_i and ε_i represent the hygroscopicity parameter and volume fraction of component i in the mixture, respectively, and i denotes the number of components. This κ_{inorg} represents the hygroscopicity of the inorganic aerosol components and is used as an upper-limit estimate for the total particle hygroscopicity, as organic matter (typically less hygroscopic) was not included.

4. Figures 5–6: Please explain the color-shaded regions in the plots. What do they represent (e.g., 1σ standard deviation, confidence interval, or other)?

Response: We greatly appreciate your insightful comments on our manuscript. These suggestions have helped us improve the clarity and interpretability of our results. Below we provide the revised.

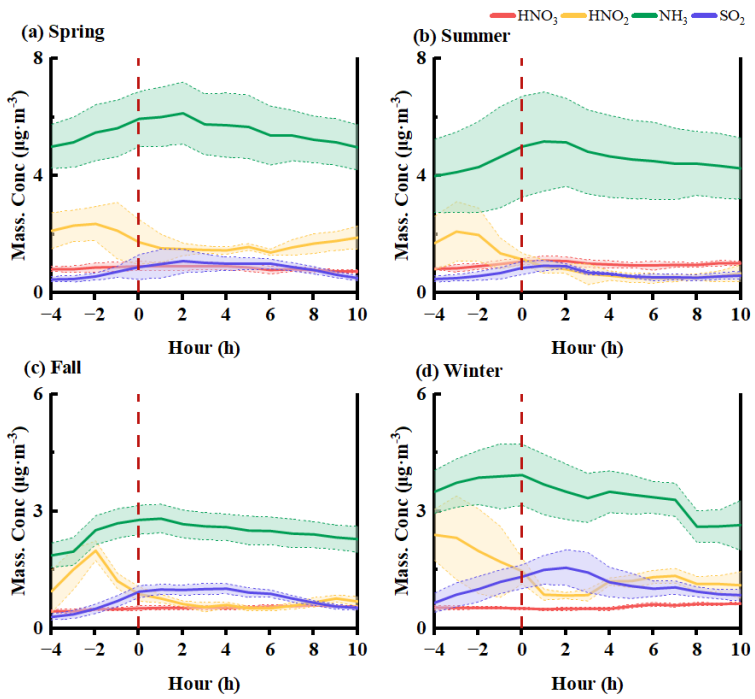

Fig. 1 The evolution of relevant trace gases (SO_2, NH_3, NO_2) before, during, and after NPF events for (a) spring, (b) summer, (c) fall, and (d) winter. The x-axis follows the same normalized time scale as defined in Fig. 4 (t=0 h represents NPF event start). Shaded bands indicate ±1σ standard deviation

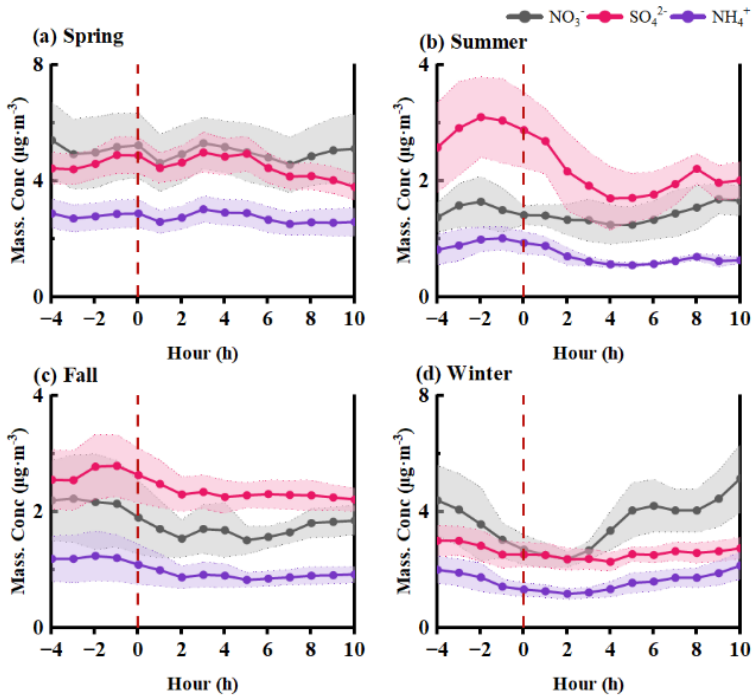

Fig. 2 The evolution of major secondary inorganic ions (SO_4^{2-}, NO_3^-, NH_4^+) before, during, and after NPF events for each season. The x-axis follows the same normalized time scale as defined in Fig. 4 (t=0 h represents NPF event start). Shaded regions represent ±1σ standard deviation across events

5. Sections 3.2 and 3.3: The results are presented by sequentially listing findings for the four seasons. Condensing this portion and adding a concluding paragraph at the end of each section that summarizes the key observations and seasonal differences would help readers better grasp the results of the study.

Response: We greatly appreciate your insightful comments on our manuscript. These suggestions have helped us improve the clarity and interpretability of our results. Below we provide the revised.

Line 358-361: In summary, spring shows the highest FR (7.13 $cm_{-3}\cdot s^{-1}$) but the lowest GR (3.69 $nm\cdot h^{-1}$) due to a large CS, indicating strong nucleation yet suppressed growth. Summer achieves the highest GR (peak 11.68 $nm\cdot h^{-1}$) and the cleanest background (lowest CS), where growth dominates over formation. Fall and winter exhibit low FR and GR with delayed growth, reflecting weaker NPF intensity.

Line 437-440: In summary, in spring, high NH_3 and photochemistry drive strong

nucleation, but high CS and secondary inorganic salts suppress growth. Summer marine air masses provide low CS and high hygroscopicity (κ_{inorg} > 0.6), favoring efficient growth, while fall and winter continental emissions (BC, POC) lower κ_{inorg} ($\leqslant$0.55) and limit NPF intensity.

6. Line 277: The phrase "Before the NPF event" is ambiguous. Does it refer to "before 9 a.m."? Please specify the time. Also, clearly define t = 0 on the x-axis of Figures 4–6.

Response: We thank the reviewer for pointing out this ambiguity. In our analysis, all NPF events were aligned by their start time (defined as the time when the nucleation-mode particle number concentration begins a sustained increase and a new mode appears in the size distribution). This start time is denoted as t = 0 h on the x-axis of Figures 4–6 and in the related text. The time window from t = –4 h to t = 0 h represents the 4 hours before the NPF event, and t = 0 h to t = 10 h represents the 10 hours after the onset of the event.

Following the reviewer's suggestion, we have added a clear explanation of this normalized time axis directly into the caption of Figure 4, as this is the most prominent figure showing time-dependent NPF parameters. The revised caption is as follows:

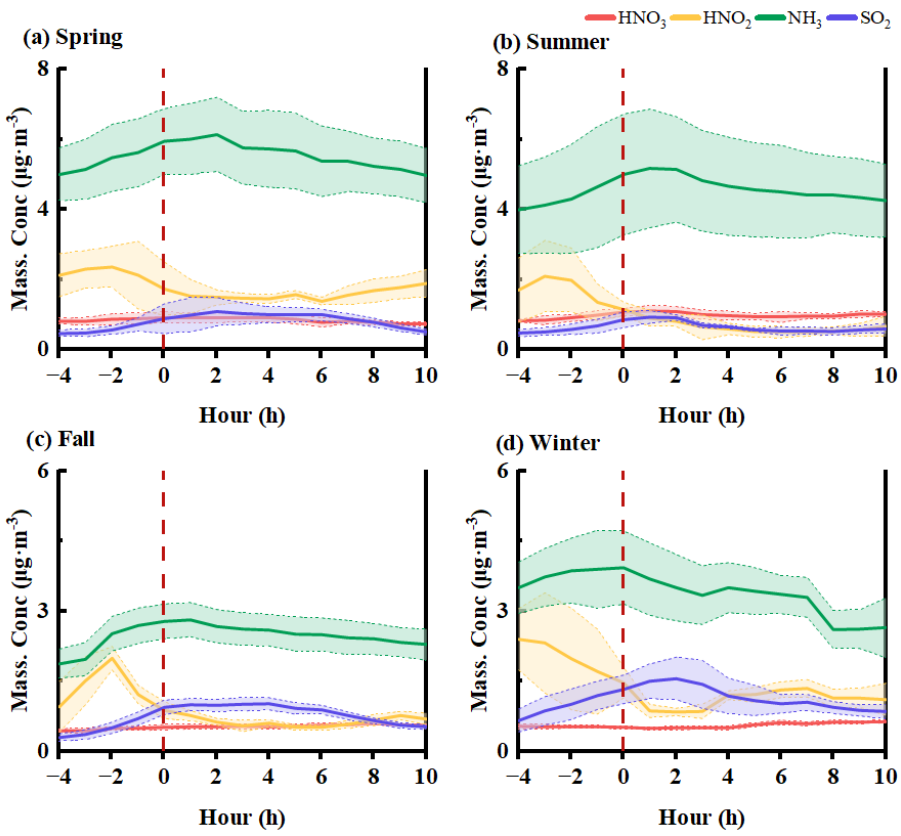

Fig. 3 The evolution of relevant trace gases (SO_2, NH_3, HNO_2, HNO_3) before, during, and after NPF events for (a) spring, (b) summer, (c) fall, and (d) winter. The x-axis follows the same normalized time scale as defined in Fig. 4 (t=0 h represents NPF event start). Shaded bands indicate ±1σ standard deviation

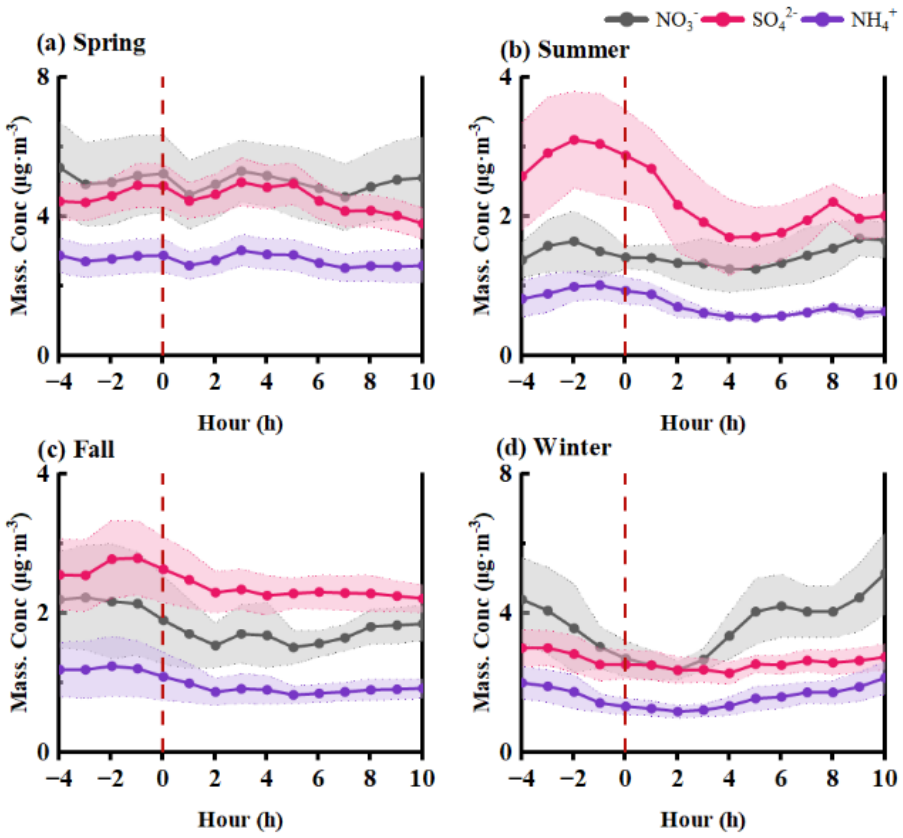

Fig. 4 The evolution of major secondary inorganic ions (SO_4^{2-}, NO_3^-, NH_4^+) before, during, and after NPF events for each season. The x-axis follows the same normalized time scale as defined in Fig. 4 (t=0 h represents NPF event start). Shaded regions represent ±1σ standard deviation across events

7. Lines 302–312: The introduction and site description note that the locations are significantly influenced by sea–land breeze circulation. Although wind shifts are briefly mentioned for summer events, a more systematic analysis would be insightful. For example, could seasonal patterns in condensation sink (CS) and precursor delivery be partly explained by prevailing wind direction (marine vs. continental) and the strength of sea–land breezes in different seasons? A brief discussion explicitly linking the observed meteorological data (wind speed/direction) to seasonal NPF characteristics would add depth to the mechanistic analysis.

Response: We thank the reviewer for the constructive suggestion to provide a more systematic analysis linking air mass origins, sea-land breeze circulation, and seasonal variations in CS and precursor delivery. In response, we performed HYSPLIT backward

trajectory clustering (72 h, 1000 m) specifically for NPF days in each season. The results are now added in Section 3.3 (with supporting figures and tables in the Supplementary Material).

In summer, after NPF onset, the wind direction shifts sharply from northwesterly land breezes to northeasterly/easterly sea breezes. At 2 h, the frequency of marine winds surges to 50%, reaching 100% at 9 h. This wind shift reduces the CS to its seasonal minimum ($1.08 \pm 0.31 \times 10^{-2}\ s^{-1}$), creating a low-sink window that enables efficient growth. Subsequently, at +3 h, κ_{inorg} increases to 0.75 (matching marine CL3), confirming that the sea-land breeze is the primary physical trigger for summer NPF. In spring, unlike summer, the wind frequency in the NE/SE coastal sectors remains stable throughout the events, with marine/coastal air already accounting for 39.1% before NPF onset. This corresponds to CL2 (coastal pathway), which supplies a sustained high concentration of NH_3 ($6.76\ \mu g \cdot m^{-3}$), sufficient to overcome the high seasonal CS ($4.1 \times 10^{-2}\ s^{-1}$), leading to high particle formation efficiency. In winter, the large-scale northwesterly monsoon (CL1) dominates the background, carrying high BC ($1.86\ \mu g \cdot m^{-3}$). However, the air mass is never fully replaced; by +10 h, northwesterly winds return to 100%, and Cl 1 exhibits high κ_{inorg} (0.59), driving late-stage nitrate-dominated growth via cold condensation. In fall, Initial northwesterly winds (62.5% at -2 h) come from continental Cl 2 and 3, providing a favorable temperature (about 22 °C) and low CS. The subsequent southerly shift (44.4% at 2 h) introduces high-humidity air (RH > 71%), although the large-scale circulation remains dominated by continental air masses.

In summary, in spring and summer, NPF is significantly influenced by sea breezes (sea-land breeze replacement in summer, stable coastal transport in spring), which play a key role in reducing CS or supplying precursors. In fall and winter, although local winds occasionally blow from marine directions, the air-mass clustering analysis shows that the large-scale circulation is still governed by continental air masses, with local sea breezes playing only a limited modulating role.

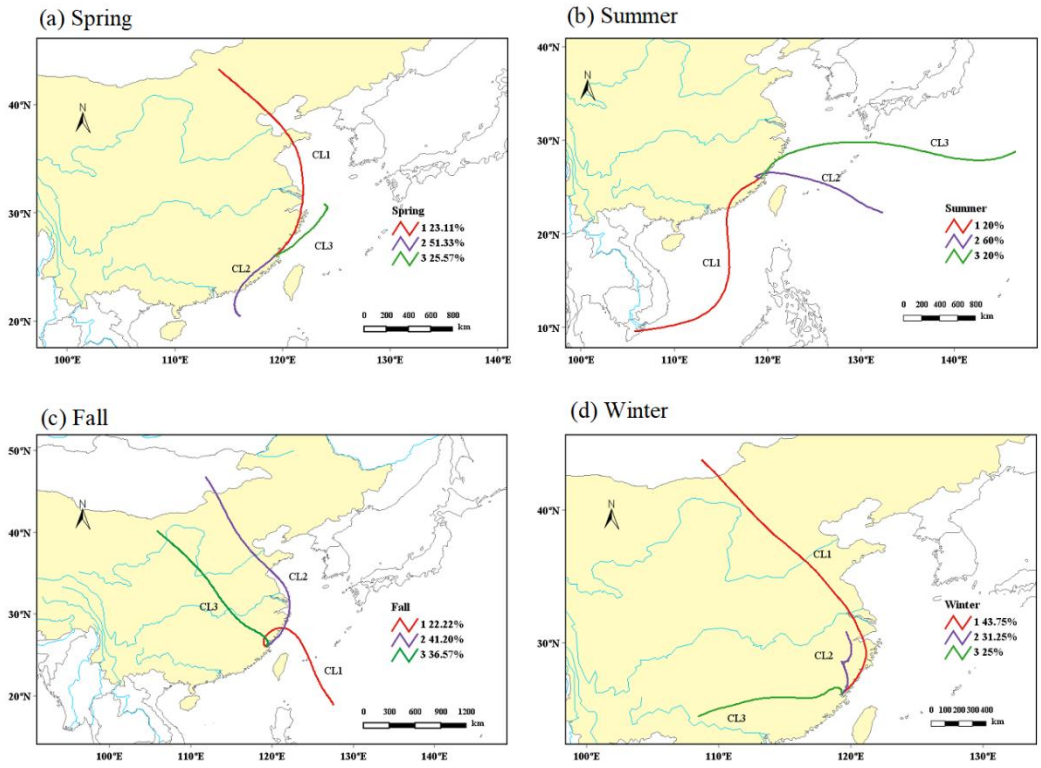

Fig.S8 Seasonal cluster analysis of 72-h back trajectories arriving at the Fuzhou site during NPF event days.

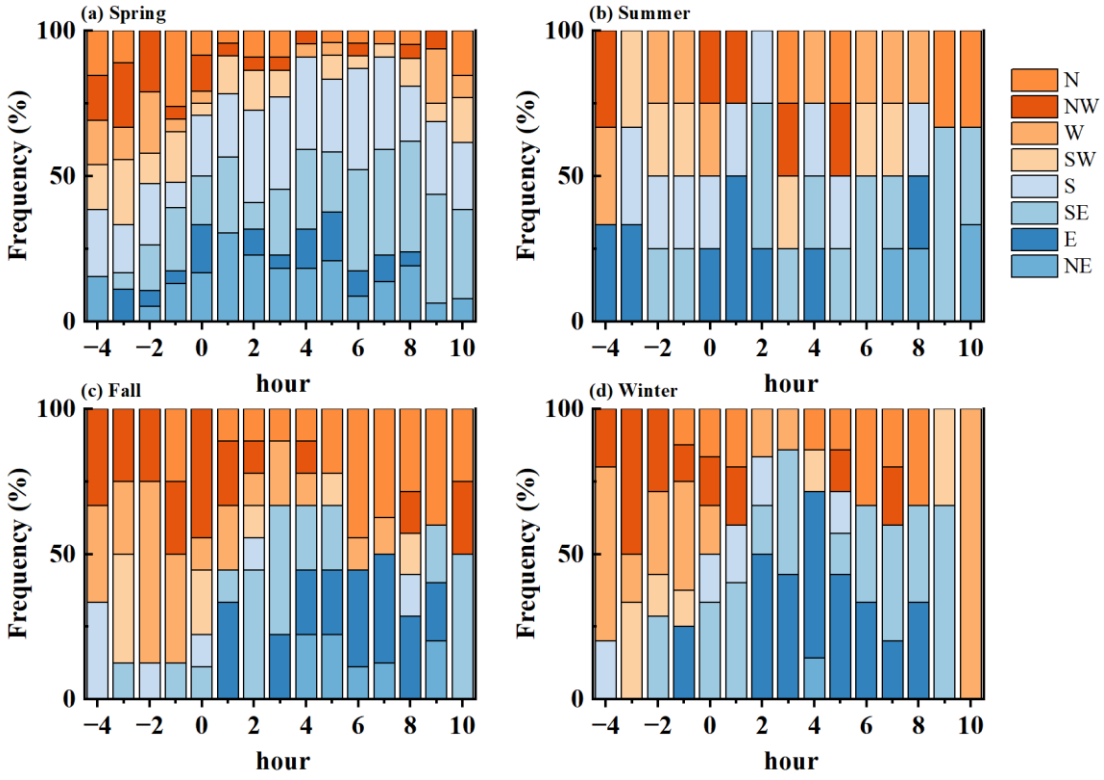

Fig.S9 Normalized diurnal frequency distribution of local wind directions surrounding NPF

onset (t=0 h) for different seasons. Time zero (0 h) marks the onset of the NPF event, with negative and positive values indicating hours before and after the onset. The eight wind sectors are color-coded, with warm colors representing continental origins and cool colors representing marine/coastal origins.

Table S3. Seasonal mean values (± standard deviation) of key NPF parameters (κ_{inorg}, Q, C, GR, CS, CoagS, and FR) for each trajectory cluster. The cluster proportion (%) is given in parentheses.

Season	Cluster (%)	κ_{inorg}	Q ($\times10^5$ $cm^{-3}\cdot s^{-}$)	C ($\times10^7$ cm^{-3})	GR ($nm\cdot h^{-}$)	CS ($\times10^{-2}$ s^{-})	CoagS ($\times10^{-4}$ s^{-})	FR ($cm^{-3}\cdot s^{-}$)
Spring	CL1 (23.11)	0.55±0.03	2.23±17.12	3.30±24.31	2.41±17.75	1.95±0.54	1.37±0.65	0.16±0.27
	CL2 (51.33)	0.52±0.03	0.39±15.65	0.68±12.70	0.50±9.27	4.36±2.14	5.61±4.00	6.65±9.92
	CL3 (25.57)	0.56±0.04	9.64±24.23	4.38±12.86	3.19±9.39	2.57±1.59	3.07±3.16	2.57±5.96
Summer	CL1 (20.00)	0.51±0.01	0.80±14.08	0.40±4.89	0.29±3.57	2.49±0.52	1.13±0.22	0.04±0.11
	CL2 (60.00)	0.55±0.03	3.63±34.62	0.98±10.31	0.71±7.52	1.08±0.31	1.01±0.65	0.06±0.24
	CL3 (20.00)	0.71±0.02	1.63±13.23	0.75±9.11	0.55±6.65	1.71±0.33	1.98±0.69	0.29±0.50
Fall	CL1 (22.22)	0.53±0.03	1.11±12.33	1.06±6.83	0.77±4.99	1.92±0.66	1.29±0.55	0.05±0.41
	CL2 (41.20)	0.58±0.05	2.45±15.34	0.90±7.37	0.65±5.38	1.70±0.71	1.18±0.75	0.08±0.25
	CL3 (36.57)	0.52±0.02	1.35±13.58	0.68±5.27	0.50±3.85	2.32±0.55	1.45±0.53	0.11±0.21
Winter	CL1 (43.75)	0.59±0.03	0.84±7.23	0.49±4.91	0.35±3.58	1.50±0.50	0.98±0.33	0.08±0.14
	CL2 (31.25)	0.58±0.04	0.07±6.75	-0.06±6.52	-0.05±4.76	2.15±0.56	1.06±0.49	0.07±0.20
	CL3 (25.00)	0.58±0.05	-1.41±9.38	-1.11±6.08	-0.81±4.44	2.50±1.02	1.32±0.52	0.07±0.16

Table S4. Seasonal mean values (±standard deviation) of precursor gas concentrations (HNO_3, HNO_2, HCl, NH_3, SO_2) for each trajectory cluster.

Season	Cluster (%)	HNO_3 ($\mu g\cdot m^{-3}$)	HNO_2 ($\mu g\cdot m^{-3}$)	HCl ($\mu g\cdot m^{-3}$)	NH_3 ($\mu g\cdot m^{-3}$)	SO_2 ($\mu g\cdot m^{-3}$)
Spring	CL1 (23.11)	0.57±0.03	0.58±0.26	0.06±0.06	1.26±0.53	1.27±1.10
	CL2 (51.33)	0.95±0.38	2.81±2.16	0.13±0.09	6.76±2.09	0.46±0.37
	CL3 (25.57)	0.66 ±0.14	1.38±1.39	0.09±0.06	4.00±1.76	0.71±0.48
Summer	CL1 (20.00)	1.22 ±0.36	1.92±1.26	0.25±0.12	7.44±1.26	0.62±0.33

	CL2 (60.00)	0.95±0.10	0.61±0.22	0.22±0.06	2.85±0.34	0.56±0.17
	CL3 (20.00)	0.93±0.07	0.49±0.08	0.23±0.05	2.98±0.24	0.53±0.07
	CL1 (22.22)	0.68±0.08	0.96±0.60	0.10±0.07	3.13±0.68	0.59±0.34
Fall	CL2 (41.20)	0.48±0.06	0.70±0.54	0.07±0.04	2.09±1.16	0.71±0.51
	CL3 (36.57)	0.50±0.08	1.08±0.87	0.06±0.02	2.59±0.57	0.83±0.32
	CL1 (43.75)	0.49±0.05	0.81±0.37	0.08±0.06	3.24±1.20	1.15±0.69
Winter	CL2 (31.25)	0.57±0.08	1.22±0.68	0.08±0.04	3.59±1.13	1.22±0.88
	CL3 (25.00)	0.58±0.09	2.36±2.83	0.07±0.04	3.83±2.73	0.92±0.64

8. Temperature and humidity effects: The text notes that high summer temperatures (>32°C) may inhibit nucleation (line 303), while lower fall temperatures (~22°C) appear favorable (lines 314–315). High relative humidity (RH >71%) in fall is also suggested to promote nucleation, likely by enhancing the uptake and hydration of sulfuric acid, a key nucleating precursor. These are valuable observations. Could the authors briefly expand the discussion, perhaps in a dedicated paragraph, to better quantify the impacts of temperature and RH? Specifically, elaborating on how temperature concurrently influences nucleation (FR) and condensable vapor production (affecting GR), and how RH modulates both initial nucleation probability and the subsequent CCN activation efficiency of grown particles, would provide a more complete picture of meteorological controls on the NPF–CCN lifecycle.

Response: We thank the reviewer for the valuable suggestion to quantify the impacts of temperature and RH on the NPF–CCN lifecycle. In response, we conducted an interpretable machine learning analysis using XGBoost (Extreme Gradient Boosting) combined with SHAP. The XGBoost model was trained to predict the observed nucleation rate (FR, 1.5–3nm particles) from multiple predictors, including temperature (T), RH, condensation sink (CS), and precursor gases (NH3, SO2). SHAP then attributes the model's output to each feature on a per-prediction basis, allowing us to extract nonlinear thresholds and interaction strengths directly from field data without

assuming a predefined functional form. This approach is increasingly used in atmospheric science to disentangle complex, interacting drivers.

The SHAP dependence plot for temperature reveals a unimodal, bell-shaped response: FR receives the strongest positive contribution in the 20–25°C range (SHAP ≈ +0.01), with contributions turning negative below 18 °C and above 28 °C, and strong suppression above 32°C (SHAP decreases by ~40% relative to the peak). This reflects a thermodynamic trade-off: moderate fall temperatures (22 °C) reduce the evaporation rate of H_2SO_4–NH_3 clusters, enhancing net FR, whereas summer heat (>32 °C) increases cluster volatility and inhibits nucleation. For the subsequent growth rate (GR) to CCN-active sizes, higher temperatures (25–30 °C) can enhance the production of condensable vapors (e.g., oxygenated organics), which may increase GR even as FR declines. We have explicitly discussed this trade-off in the revised manuscript. Regarding RH, contrary to the initial suggestion that high RH (>71%) promotes nucleation, our SHAP analysis shows a predominantly monotonic negative contribution of RH to FR (SHAP decreasing from +0.2 at RH≈50% to –0.6 at RH>71%). The apparent high-RH–high-FR correlation in fall is likely due to covariation with lower T and lower CS. Mechanistically, high RH suppresses nucleation via (i) reduced photolytic H_2SO_4 production under increased cloud cover, and (ii) enhanced CS from hygroscopic growth of pre-existing particles. However, once particles grow to ~30–50 nm, high RH strongly improves their CCN activation efficiency (Köhler theory). This dichotomous role of RH — suppressing nucleation but promoting activation — is now articulated in a dedicated paragraph, and we identify an optimal balance for net NPF–CCN yield at 50–65% RH combined with 20–25 °C.

Although the reviewer focused on T and RH, our SHAP analysis also yielded a novel, site-specific finding regarding precursor gases, which we have added to complement the meteorological discussion. NH_3 contributes approximately 2.1 times more to FR than SO_2 (1.3% vs. 0.6% of explained variance), and exhibits a sharp threshold at 4 μg m^{-3}. Below this value, NH_3 suppresses nucleation (SHAP negative); above it, the

SHAP contribution turns positive and rises steeply (+0.2 at 10 $\mu g \cdot m^{-3}$). This quantitatively identifies Fuzhou as an NH_3-limited nucleation regime. All of the above quantitative results are now presented in a new subsection (Section 3.4) with two new figures (SHAP dependence plots for T, RH, and NH_3; interaction matrix).

Section 3.4:

3.4 Attribution analysis of particle formation and growth

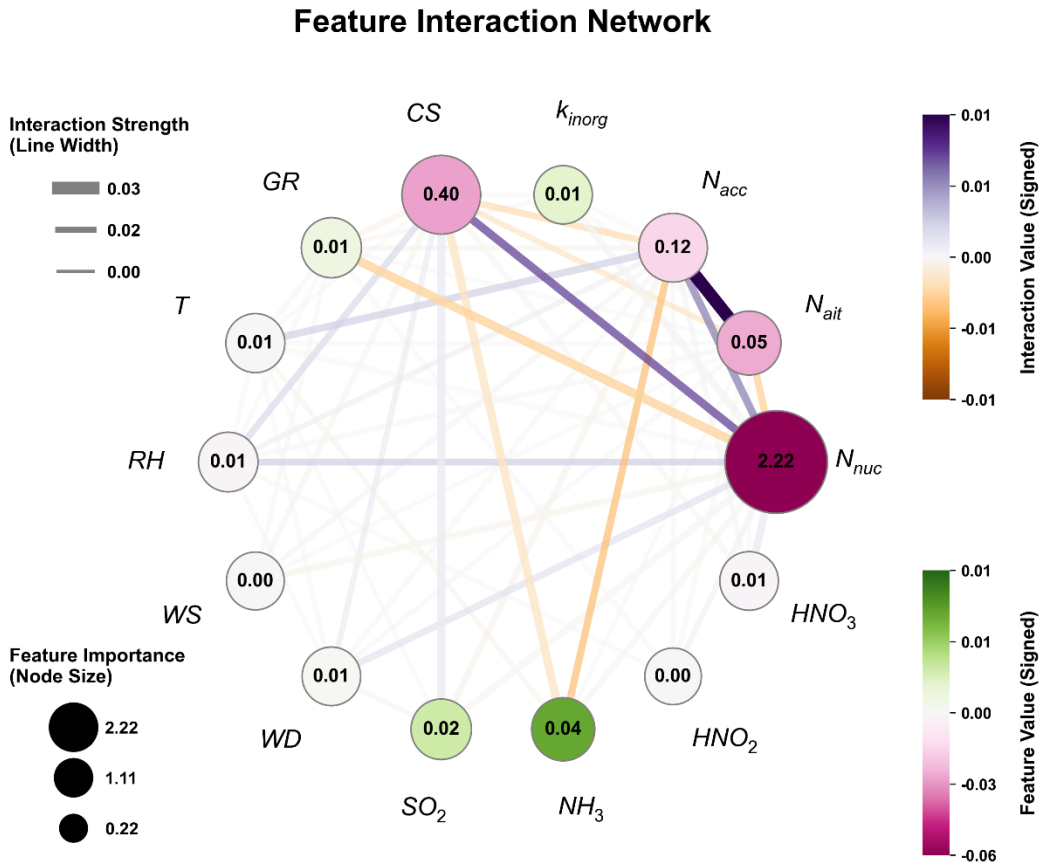

Fig. 5 Non-linear response relationships and interaction analysis between core environmental factors and FR. Node size and inner numbers denote feature importance (mean |SHAP|). Node color indicates contribution direction (green: positive; pink: negative). Edge width reflects interaction strength; edge color indicates interaction direction (purple: synergistic; orange: antagonistic).

According to SHAP analysis (Fig.S14), the main contributors to FR in Fuzhou are nucleation mode (76.2%), CS (13.8%), NH_3 (1.3%), and SO_2 (0.6%). Physical

processes explain ~90% of the variance. A prominent feature is the sharp NH_3 threshold at 4 $\mu g \cdot m^{-3}$: below this, SHAP ≈ -0.025; above, it turns positive and rises by 0.2 at 10 $\mu g \cdot m^{-3}$. CS shows a clear inhibition onset at 0.03 s^{-1}, with SHAP dropping from 0 to -0.5 as CS increases to 0.08 s^{-1}. Temperature has a positive SHAP only within 20–25°C (peak ~0.01), decreasing by 40% at 35°C. As shown in Fig. 7, the strongest interaction is between nucleation mode and CS (0.40), far exceeding other pairs (NH_3-nucleation mode: 0.04), highlighting that the net FR is governed by the competition between particle formation and scavenging.

For the Aitken mode, the driving forces shift notably. CS remains the top contributor, followed by accumulation mode (13.8%) and nucleation mode (7.1%). As shown in Fig.S15, a key distinction from FR is the temperature response. Instead of a bell shape, SHAP increases linearly from 0 to 0.1 over 20–35°C, indicating that high temperatures accelerate particle growth, enabling a rapid transition from nucleation to the Aitken mode. The NH_3 threshold at 4 $\mu g \cdot m^{-3}$ persists, showing its continued role in particle growth. RH exerts a linear negative effect, turning SHAP negative above 60%, suggesting hygroscopic growth or coagulation loss. In Fig.S16, the CS–nucleation mode interaction strength is 0.12, lower than in FR but still dominant, implying that strong nucleation can offset high CS losses.

In summary, the SHAP attribution reveals two distinct regimes. FR is dominated by CS, accompanied by a sharp chemical trigger (NH_3 >4 $\mu g \cdot m^{-3}$) and a narrow temperature window (20–25°C). The Aitken mode, while still influenced by CS, is primarily driven by temperature-accelerated growth (linearly increasing above 20°C). Ammonia acts as a persistent enhancer in both stages, whereas high RH (>60%) consistently suppresses Aitken mode concentrations.

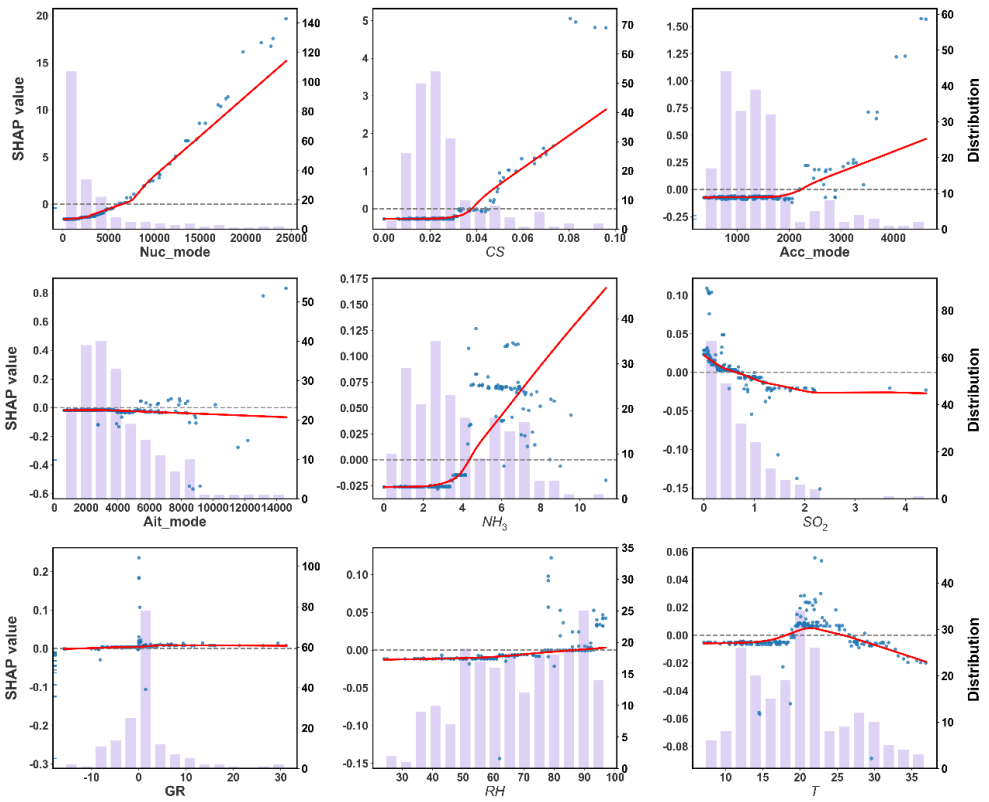

Fig.S14 Global importance analysis of influencing factors for particle formation rate (FR) based on SHAP summary plot.

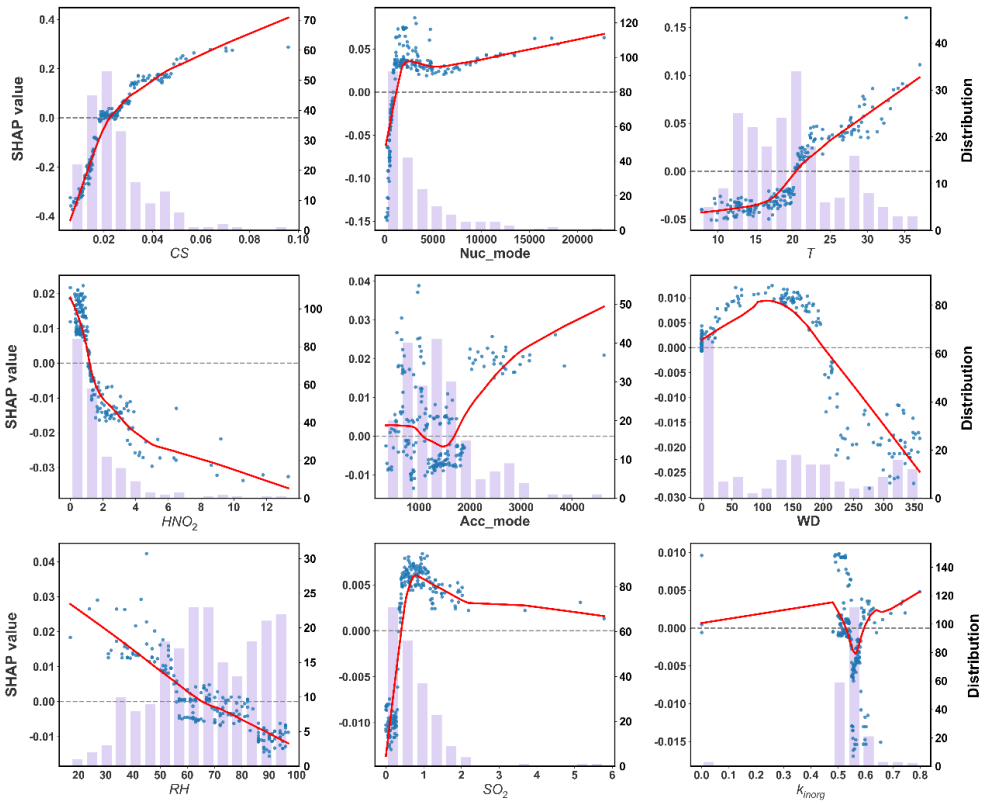

Fig.S15 Global importance analysis of influencing factors for N_{ait} based on SHAP summary plot.

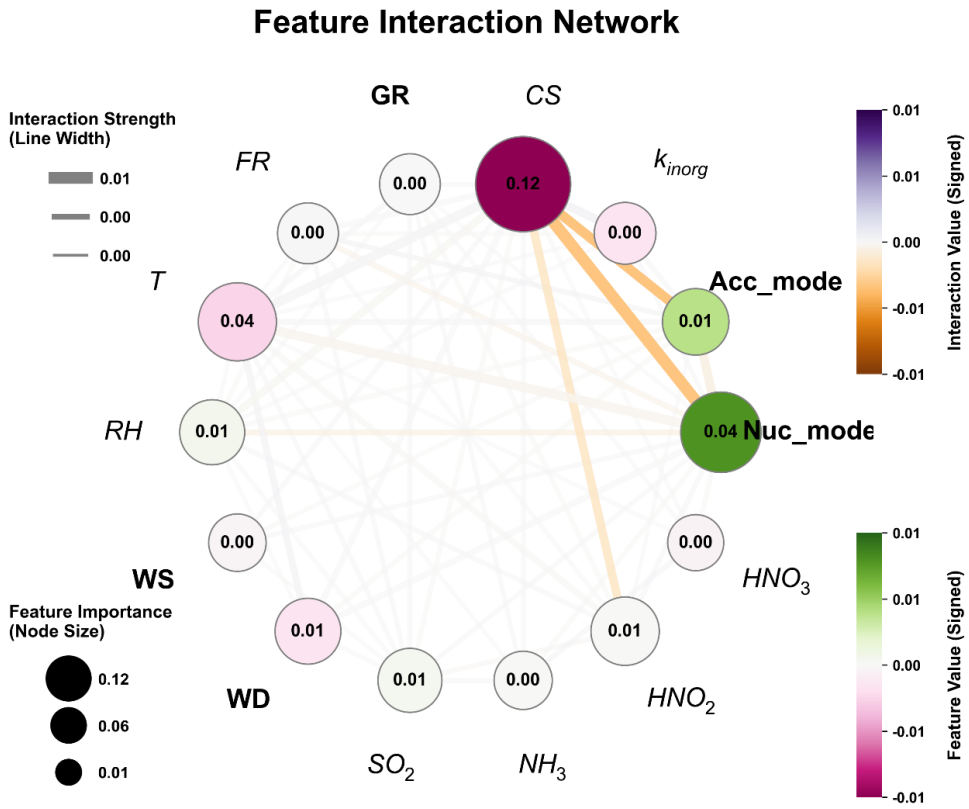

Fig.S16 Non-linear response relationships and interaction analysis between core environmental factors and N_{ait}.